# High-resolution numerical simulations of the convective system observed in the Lago Maggiore area on 17 September 1999 (MAP IOP 2a)

Evelyne Richard, Stéphanie Cosma, Pierre Tabary, Jean-Pierre Pinty, Martin Hagen

▶ **To cite this version:**

Evelyne Richard, Stéphanie Cosma, Pierre Tabary, Jean-Pierre Pinty, Martin Hagen. High-resolution numerical simulations of the convective system observed in the Lago Maggiore area on 17 September 1999 (MAP IOP 2a). Quarterly Journal of the Royal Meteorological Society, 2003, 129, pp.543-563. 10.1256/qj.02.50 . hal-00136956

**HAL Id: hal-00136956**
**https://hal.science/hal-00136956**

Submitted on 12 Nov 2020

**HAL** is a multi-disciplinary open access archive for the deposit and dissemination of scientific research documents, whether they are published or not. The documents may come from teaching and research institutions in France or abroad, or from public or private research centers.

L'archive ouverte pluridisciplinaire **HAL**, est destinée au dépôt et à la diffusion de documents scientifiques de niveau recherche, publiés ou non, émanant des établissements d'enseignement et de recherche français ou étrangers, des laboratoires publics ou privés.

Distributed under a Creative Commons Attribution - NonCommercial 4.0 International License

# High-resolution numerical simulations of the convective system observed in the Lago Maggiore area on 17 September 1999 (MAP IOP 2a)

By EVELYNE RICHARD[1]*, STEPHANIE COSMA[2], PIERRE TABARY[3], JEAN-PIERRE PINTY[1] and MARTIN HAGEN[4]

[1]*Laboratoire d'Aérologie, CNRS and Université Paul Sabatier, Toulouse, France*
[2]*CNRS and Université Pierre et Marie Curie, Paris, France*
[3]*Centre d'étude des Environnements Terrestre et Plantétaires, CNRS, Velizy, France*
[4]*Institut für Physik der Atmosphäre, DLR, Oberpfaffenhofen, Germany*

SUMMARY

During Intensive Observing Period (IOP) 2a of the Mesoscale Alpine Programme (MAP) a significant convective system developed in the Lago Maggiore area. Its evolution is simulated using the Meso-NH model run over three nested domains with a 2 km horizontal resolution for the finest grid. Model results are assessed by comparing computed precipitation and model radar reflectivities with observed parameters. A control simulation initialized with European Centre for Medium-Range Weather Forecasts analyses and run with the standard microphysical scheme of the model yields fairly realistic results. Neglecting the ice processes in the microphysical scheme degrades the numerical results, whereas, significant improvement is obtained when heavy rimed particles are considered to be hail instead of graupel.

KEYWORDS: Mesoscale Alpine Programme Orography Precipitation Radar

## 1. INTRODUCTION

In recent years, substantial progress has been achieved in the field of numerical weather modelling. Modern computer systems have provided the technical capacity for developing fine-grid models with resolutions as low as a few kilometres. Such high-resolution models are currently under intensive testing in many research institutions and foreshadow the next generation of operational weather-forecast systems.

At high resolution, convection is explicitly resolved, meaning that clouds and precipitation are entirely represented through additional prognostic equations which account for the microphysical and thermodynamical transformations associated with water phase changes. Moreover, high resolution allows for a much more detailed representation of the orographic forcing, known to play a major role at the mesoscale. One major expectation from these new numerical tools is a better forecast of small-scale meteorological phenomena such as thunderstorms, squall lines, or convective rain bands, and a more reliable estimate of associated precipitation (Lilly 1990). However, little experience has been gained so far in concluding to what extent such phenomena are predictable.

To provide a database suited for the evaluation of high-resolution models was one central objective of the Mesoscale Alpine Programme (MAP, Bougeault *et al.* 2001). Within the two-month MAP field campaign, some 15 heavy-to-moderate precipitation events were documented on the southern slopes of the Alps. Among them, the episode observed on 17 September 1999 during the Intensive Observing Period (IOP) 2a was not the most intense in terms of precipitation (70 mm) but was certainly the episode during which convection developed the most, with cloud tops reaching 12 km and many lightning impacts recorded at the ground. In real time, this precipitating event was badly forecast even with the high-resolution Canadian model MC2 (Benoit *et al.* 1997; Benoit *et al.* 2002) running with a 3 km resolution.

* Corresponding author: Laboratoire d'Aérologie, 14 Avenue E. Belin, F-31400 Toulouse, France.
e-mail: rice@aero.obs-mip.fr

This case was selected to evaluate the performance of the Meso-NH model, recently developed in the French community. This model integrates a non-hydrostatic system of equations, uses a two-way interactive grid-nesting technique, and includes a fairly detailed representation of clouds and precipitation.

This paper presents the results of different numerical simulations aiming to identify the strengths and weaknesses of this model. Available observations of the event are described in section 2. The model characteristics and the numerical set-up are presented in section 3. Section 4 is devoted to the analysis of the simulation results, whereas a quantitative assessment of simulated precipitation is given in section 5. The final section provides a conclusion and outlook.

## 2. Observations

### (*a*) *Synoptic situation*

This section briefly describes the meteorological situation of the event based on the European Centre for Medium-Range Weather Forecasts (ECMWF) analyses. The analysed mean sea-level pressure, surface wind, 500 hPa geopotential and wind are presented in Fig. 1 for 17 September 1999 at 12 UTC. At the surface, a 982 hPa low is located 15° west of Ireland, whereas, a secondary low (1004 hPa) stands over the Italian peninsula and induces a rapid flow (10 m $s^{-1}$) over the Adriatic Sea towards north-western Italy. The 500 hPa chart shows a ridge extending from Hungaria to Scandinavia and a trough from Ireland to western Spain. Notice in between, the presence of a short-wave trough over southern France. As this feature progresses eastward, the atmosphere over northern Italy is destabilized by upper-level cold and moist advection. This is quite noticeable in the time evolution of the Milano sounding between 12 and 18 UTC (see Fig. 2). At 18 UTC, the convective available potential energy (CAPE) is moderate, but the vertical thermodynamical structure is now propitious for deep convective development. The wind profile varies from a south-easterly flow at low level to a south-westerly flow at 500 hPa. This feature is commonly observed for precipitation events in the Lago Maggiore region (Houze *et al.* 2001).

### (*b*) *Radar observations*

During the MAP field experiment, special efforts were devoted to obtaining radar observations. At the scale of the Alpine massif, a radar composite combining the data of operational radar networks from Austria, France, Germany and Switzerland was routinely generated in quasi real time (Hagen 1999). The radar-derived precipitation rates originating from the different operational weather services were re-mapped on a common polar-stereographic grid (with a 2 km × 2 km mesh) covering the whole Alpine area. The four panels of Fig. 3 span 18 hours and depict the time evolution of the precipitation pattern observed in the evening and early night of 17 September 1999. A wide band of north–south elongated precipitation developed ahead of the upper-level trough, propagated eastward and was quite reinforced when crossing the Alps. At 21 UTC, precipitation rates in excess of 100 mm $h^{-1}$ were found over north-eastern Italy, south of the Swiss Ticino.

A close-up look at the event can be obtained from the special radar network that was set up for MAP in the Lago Maggiore region. During the MAP IOPs, this area was monitored by a ground-based Doppler-radar network composed of the American S-band polarimetric radar S-Pol from the National Center for Atmospheric Research, the French C-band research radar RONSARD, and the MeteoSwiss's C-band operational radar from Monte Lema in Ticino (see Fig. 5(b) for their location). These radars provided

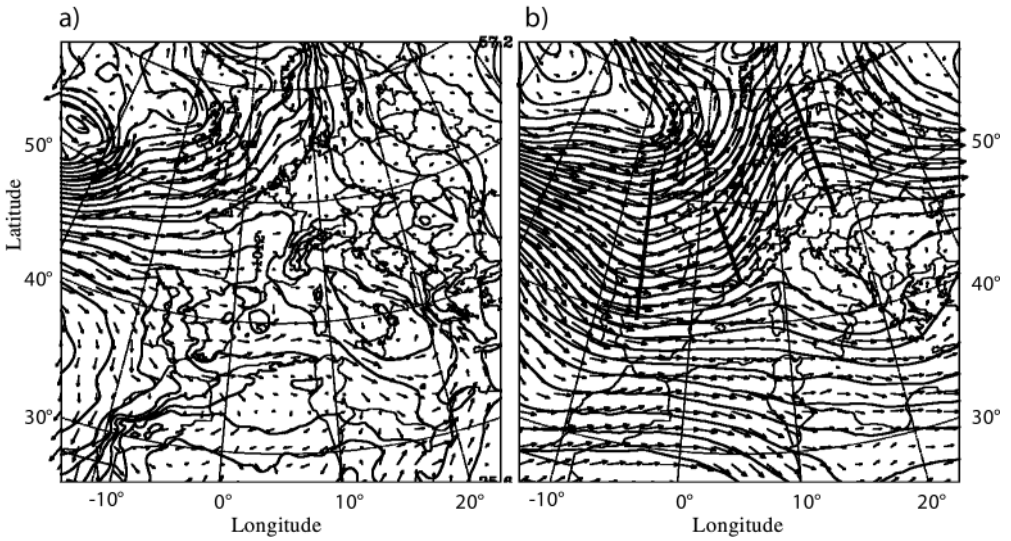


Figure 1. Synoptic situation of 17 September 1999, 12 UTC as diagnosed by the ECMWF operational analysis. (a) Mean sea-level pressure (contours every 2 hPa) and surface wind vectors. (b) 500 hPa geopotential height (contours every 20 m) and wind vectors. The thick lines in (b) indicate the locations of the trough, ridge and short-wave trough mentioned in the text.

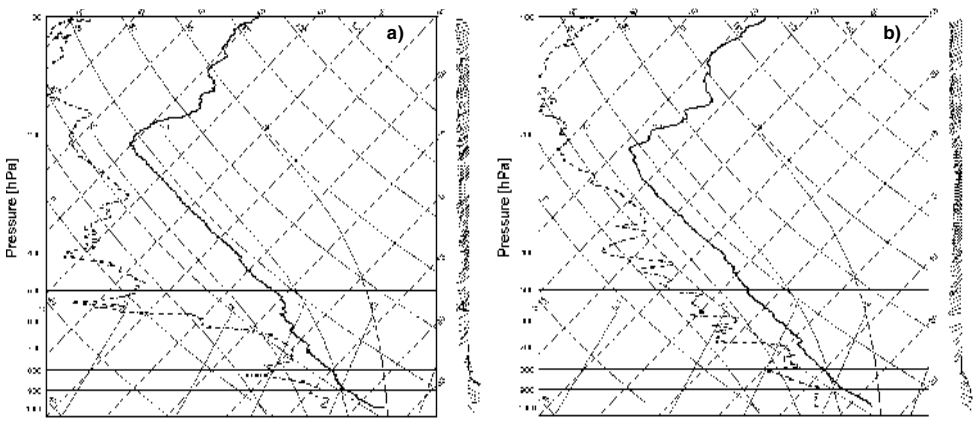


Figure 2. Milano soundings of 17 September 1999, (a) 12 and (b) 18 UTC.

dual-Doppler data allowing not only the mapping of the reflectivity field but also the retrieval of the three-dimensional wind field (Chong *et al.* 2000; Tabary 2002). Figure 4, based upon this dataset, is focused over the Lago Maggiore area and presents the time evolution of the radar reflectivity field measured at 2000 m (all heights quoted are above mean sea level), between 20 and 23 UTC, i.e. during the most intense phase of the precipitating system. In the Lago Maggiore area, the system started in the late afternoon. Around 17 UTC (not shown), isolated convective cells were initiated on the Alpine slopes. Then between 19 and 20 UTC these cells merged into a well defined convective line oriented north-east–south-west which then propagated south-eastward. Later in the evening (21 UTC), further convection developed ahead of the initial line

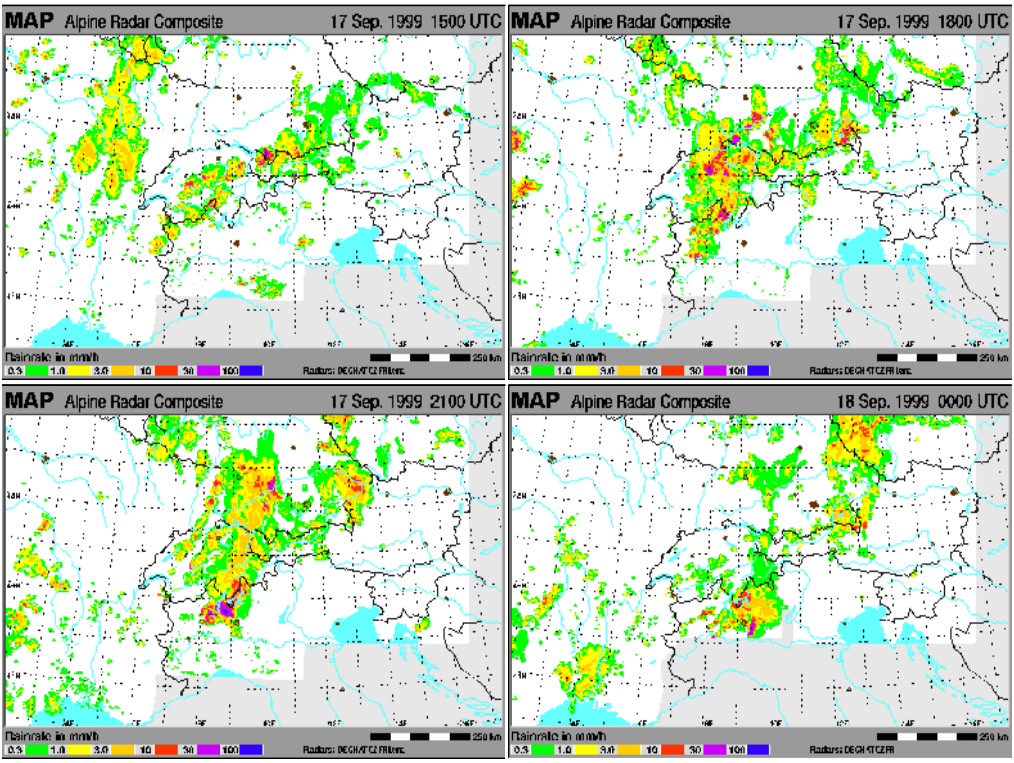


Figure 3. Precipitation rate (mm $h^{-1}$) from the Alpine radar composite: time evolution from 17 September 1999, 15 UTC to 18 September 1999, 00 UTC. (This figure can be seen in colour in the online version.)

making the system more complex and definitively three dimensional. It then continued to propogate eastward and left the observation area after midnight. The maximum intensities are around 50 dBZ with occasional local peaks above 60 dBZ in the most active turrets.

## 3. Numerical simulations

### (*a*) *Model characteristics*

The simulations were carried out with the three-dimensional non-hydrostatic model Meso-NH developed jointly by Météo-France and Laboratoire d'Aérologie. The model integrates a system of equations which is based upon the Lipps and Hemler (1982) anelastic formulation. The equations are integrated in a system of curvilinear coordinates with non-uniform grids: geographic conformal projections on the horizontal plane, and a Gal-Chen and Sommerville (1975) vertical coordinate. For the spatial discretization, a C-grid in the Arakawa and Mesinger (1976) terminology is used. The temporal scheme is a three-time-level leap-frog with a time filter (Asselin 1972). The model orography is derived from a high-resolution topographical dataset, averaged over each grid mesh, and smoothed at $2\Delta x$. Horizontal diffusion is introduced by a fourth-order operator in all prognostic equations to damp the short numerical waves. Lateral boundaries are radiative or open boundary conditions. The top boundary is a rigid horizontal lid associated with an absorbing layer to prevent the reflection of gravity waves. More details about the adiabatic formulation of the model can be found in Lafore *et al.* (1998).

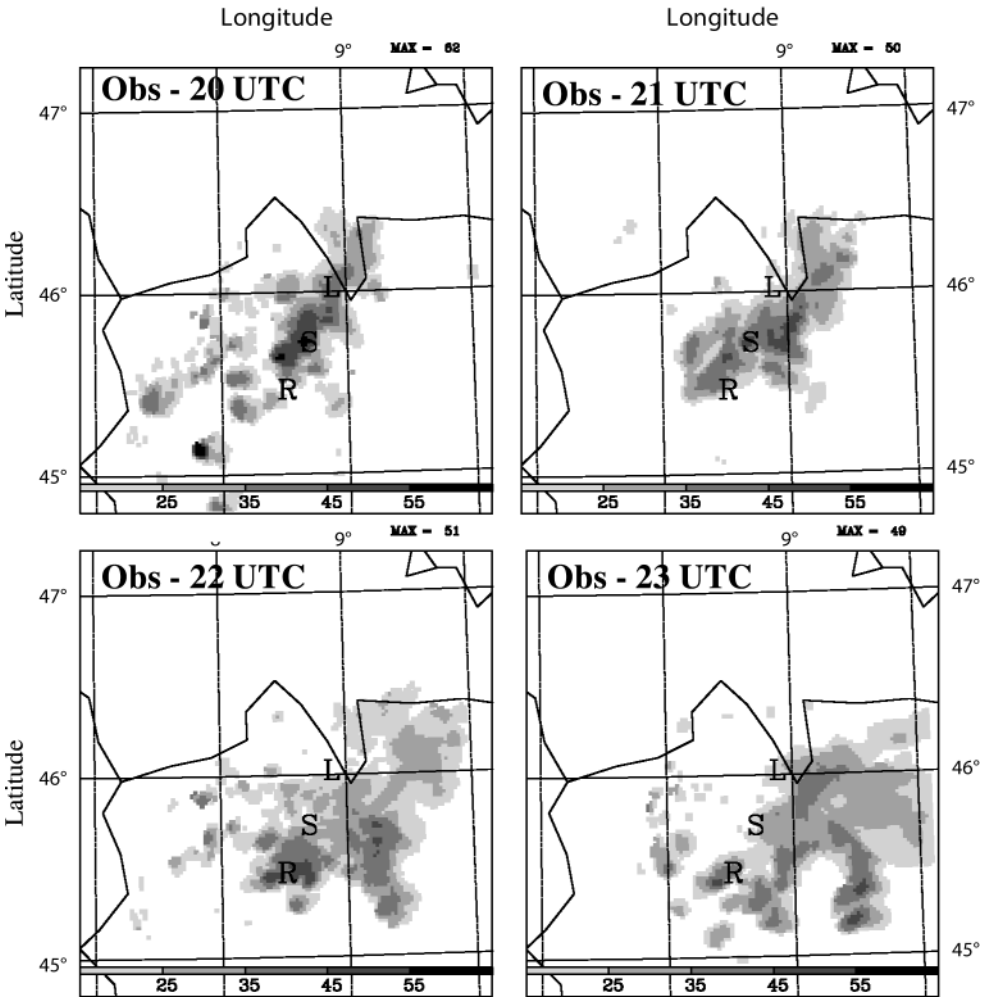


Figure 4. Observed reflectivity field (dBZ) on 17 September 1999 (20, 21, 22 and 23 UTC) at 2000 m in the Lago Maggiore area. The solid lines are a rough representation of the political borders between France, Italy and Switzerland. The locations of the Monte Lema, S-Pol and RONSARD radars are indicated by the letters L, S and R, respectively. At each grid point, the reflectivity is computed as the maximum reflectivity from the three radars.

The model contains a number of physical packages to reproduce the different atmospheric processes. The parametrizations activated for performing our simulations are: the ISBA surface scheme (Noilhan and Planton 1989), the one-and-a-half turbulent scheme based on the physical mixing length of Bougeault and Lacarrère (1989), the convection scheme (Bechtold *et al.* 2001) adapted from Kain and Fritsch (1993), the radiative scheme used at ECMWF (Morcrette 1989), and a bulk mixed-phase microphysical scheme (Pinty and Jabouille 1998).

### (*b*) *Numerical set-up*

In order to simultaneously simulate the synoptic situation over western Europe, the mesoscale forcing of the whole Alpine massif, and the detailed fine-scale structure

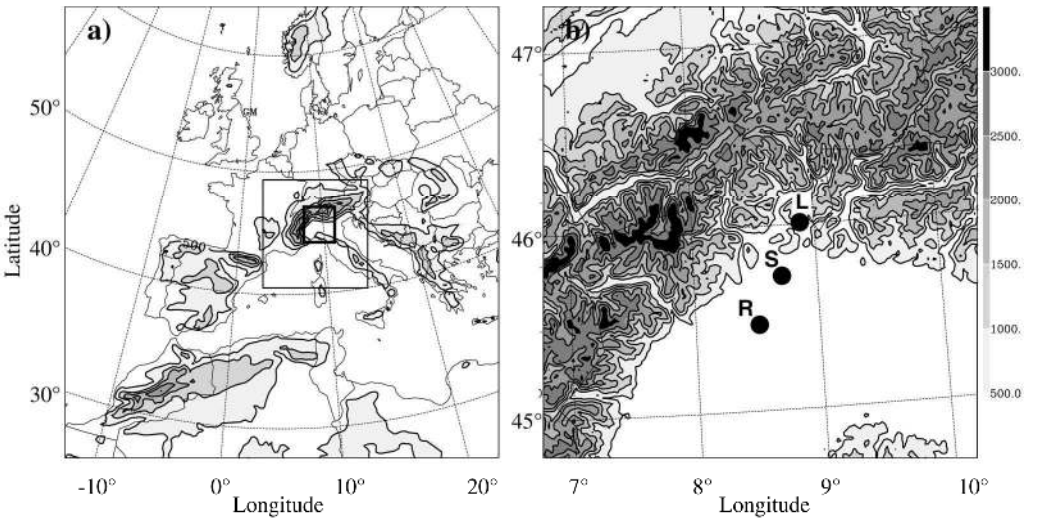


Figure 5. (a) Geographical domains used for the nested simulation. The outer frame shows the 32 km grid mesh domain and its topography, the location of the 8 km (2 km) grid mesh domain is indicated with thin (thick) lines. (b) Topography (m) of the 2 km grid mesh domain, and locations of the three radars (R, S and L for RONSARD, S-Pol and Monte Lema, respectively).

of the convective system, three levels of nesting were deemed necessary. The different horizontal meshes were set to 32, 8 and 2 km. The three simulation domains are shown in Fig. 5(a). The coarse-mesh model is large enough to capture the synoptic-scale evolution. The 8 km mesh model comprises the entire Alpine massif, whereas, the 2 km mesh domain is centred on the Lago Maggiore area. As can be seen from Fig. 5(b), most of the Alpine valleys are fairly well resolved in the 2 km mesh. The vertical grid is identical in all three domains. It has 50 levels with a mesh stretched between 60 m near the ground and 600 m at the top of the model domain at a height of 20 km.

The model simulation starts at 12 UTC on 17 September 1999 and is integrated for 12 hours with a two-way interactive grid nesting technique (Stein *et al.* 2000). Initial conditions and boundary conditions of the outermost model are obtained by interpolating the ECMWF operational analyses available every 6 hours. The physical package is the same in the three domains except for the 2 km run where the convection scheme was not activated.

Three experiments were performed and all of them were initialized and forced with the ECMWF operational analyses. The control run (E1) makes use of the standard microphysical scheme of the model which includes three categories of ice particles (pristine ice, aggregates and graupel). The other two experiments aim to study the sensitivity of the results to the microphysical scheme. Experiment E2 differs from E1 by the fact that only warm microphysical processes are accounted for, whereas, in experiment E3, the graupel characteristics are replaced by those of denser hail-like particles. This latter experiment is motivated by S-Pol observations which reveal the presence of significant amounts of hail particles especially in the early stage of the convective-line development (Tabary 2002).

Hereafter, only the results concerning the high-resolution simulations will be presented.

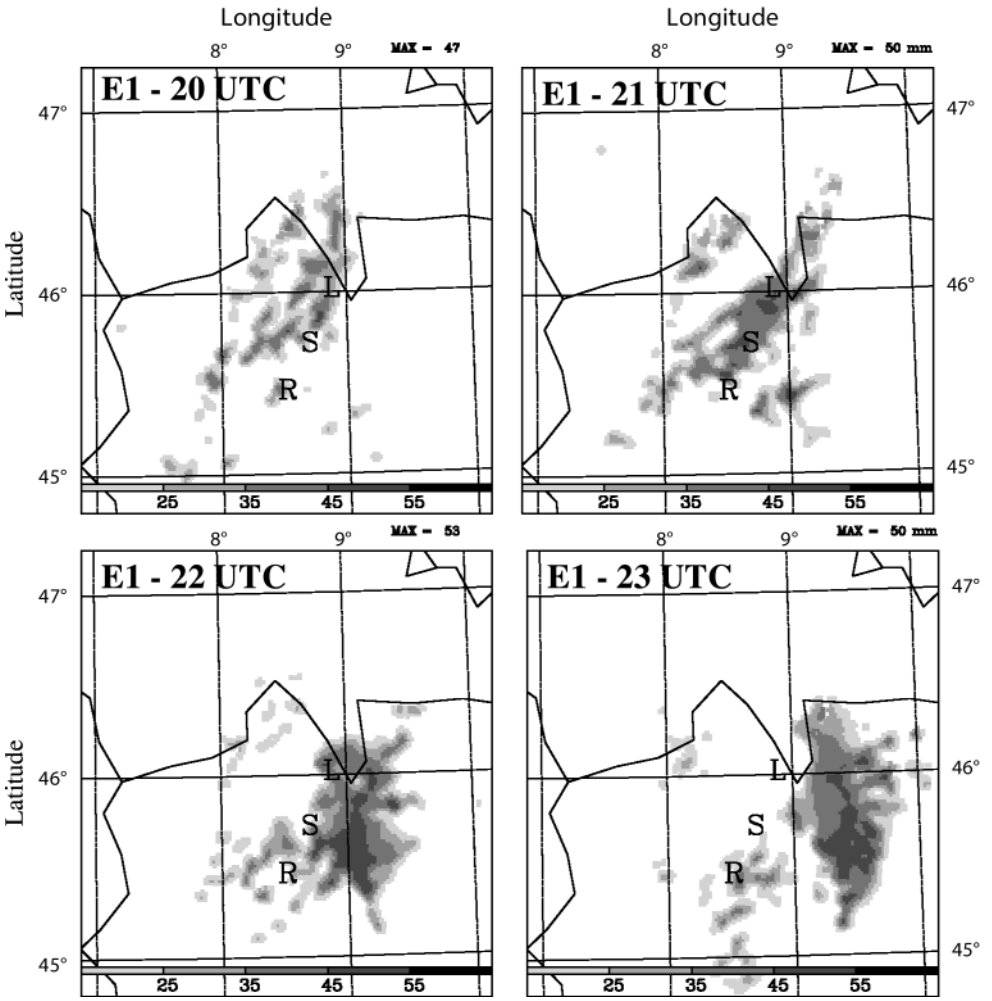


Figure 6. Computed reflectivity fields (dBZ) for 17 September 1999 (20, 21, 22 and 23 UTC) at 2000 m in the Lago Maggiore area: results of experiment E1 (see text).

## 4. Results

### (*a*) *Control experiment*

The results of the control experiment (E1) are shown in Fig. 6. To ease the comparison with the observations, pseudo radar reflectivities were computed from the model microphysical fields (see the appendix for details of the computation). To match the effective resolution of the radar fields, the model fields were smoothed by applying a Leise filter (Leise 1981). The numerical results are presented using the same plotting format as for the observations and Fig. 6 can be directly compared with Fig. 4. At the beginning of the time sequence (20 UTC), the model appears somewhat late in initiating strong convection. It underpredicts the width and intensity of the convective line but captures its location quite well. The discrepancy in the spatial extent diminishes with time but remains present throughout the whole time sequence. This is particularly true in the north-eastern edge of the system. However, the eastwards displacement of

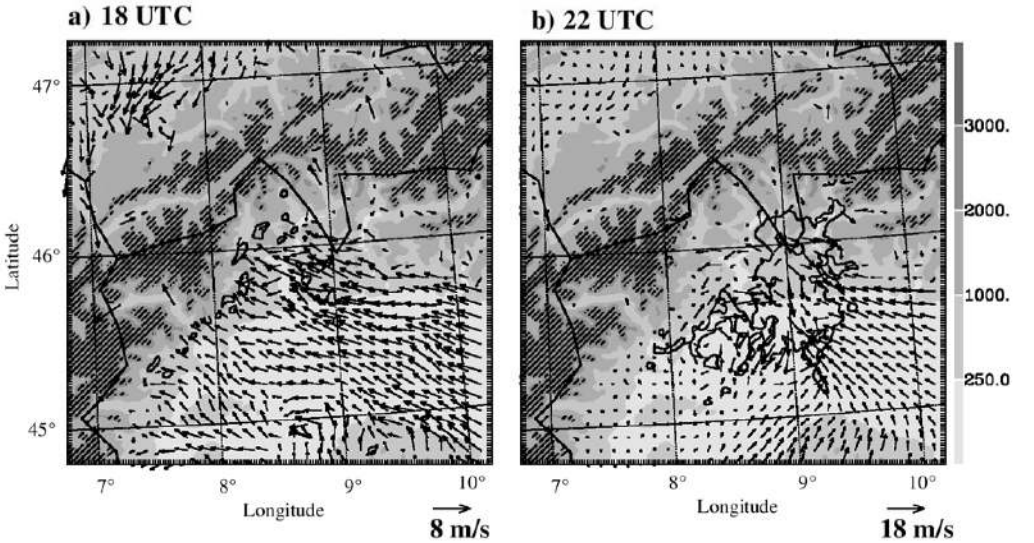


Figure 7. Computed wind field at 1000 m superimposed with the topography (m), and with the 30 dBZ contour of the reflectivity at 2000 m for 17 September 1999, 18 UTC (a), and 22 UTC (b). Notice that the vector scale is different in the two frames.

the system is quite accurately reproduced by the model. Another point of agreement between the computations and the observations is the shape modification of the system with a line pattern progressively evolving into a horseshoe-like pattern. Although this is more obvious in the observations, there is clear indication in the model fields (at 21 and 22 UTC) that a new convective area builds up east of 9° and ahead of the initial convective line.

Figure 7 gives further insight into this evolution. It shows the computed wind field at 1000 m superpimposed on the topography. The location of the precipitation is recalled by the 30 dBZ contour of the reflectivity at 2000 m. In the early stage of the system (Fig. 7(a), 18 UTC) convection occurs mainly through orographic lifting. The south-eastern flow originating from the Adriatic sea impinges the interior of the Alpine arch, and a convective line forms parallel to the slope and perpendicular to the low-level flow. Four hours later (Fig. 7(b), 22 UTC), the line has moved eastward, partly because of its own dynamics and thermodynamics but also partly because of the modifications in the environment. The flow originating from the Ligurian Sea has accelerated and rotated eastward. Strong convergence now occurs between the Ligurian and the Adriatic air streams and triggers additional convection. Three steps can be distinguished to summarize the system evolution: a first stage in which the orographic lifting plays a major role in assembling isolated cells into a convective line; a second stage during which the line propagates eastwards; and a third stage during which it merges with new convective cells triggered by the convergence of the Adriatic- and Ligurian-originating flows.

### (*b*) *Sensitivity to the microphysical scheme*

On finer-scale simulations, a larger fraction of the precipitation is explicitly resolved and increased accuracy in the microphysical scheme becomes essential. In particular, the importance of ice microphysics to the precipitation formation in convective storms has been widely stressed in recent works (Chen and Cotton 1988; McCumber

TABLE 1. COEFFICIENTS USED IN THE MASS–DIAMETER AND FALL VELOCITY–DIAMETER RELATIONSHIPS FOR THE DIFFERENT TYPES OF HYDROMETEORS

| | Pristine ice | Snow | Graupel | Hail | Raindrop |
|---|---|---|---|---|---|
| a | 0.82 | 0.02 | 19.6 | 470 | 524 |
| b | 2.5 | 1.9 | 2.8 | 3 | 3 |
| c | 800 | 5.1 | 124 | 207 | 842 |
| d | 1.00 | 0.27 | 0.66 | 0.64 | 0.8 |

These relationships are respectively given by $m = aD^b$, and $v = cD^d(\rho_o/\rho)^{0.4}$, where $m$ is the mass, $v$ is the fall velocity, $\rho$ is the air density and $\rho_o$ the air density at 1000 hPa.

*et al.* 1991; Caniaux *et al.* 1994; Chin 1994; Krueger *et al.* 1995; Yang and Houze 1995; Bielli and Roux 1999).

The standard explicit microphysical scheme of the Meso-NH model accounts for mixed-phase clouds and precipitation. The scheme predicts the mixing ratio of six atmospheric water categories: water vapour, non-precipitating and precipitating liquid water, non-precipitating ice, snow aggregates, and graupel. Precipitating particles are assumed to be distributed according to generalized gamma functions. For each particle type, mass–diameter and fall velocity–diameter relationships are expressed as power laws that can easily be adapted to any specific type of hydrometeor (see Table 1). Multiple interactions operating between the different water categories are accounted for through the parametrization of some 35 microphysical processes (nucleation, water-vapour deposition, riming, melting, sedimentation, . . . ).

Such a detailed microphysical scheme requires additional computing resources which preclude its use in operational models. In most current operational models, no more than two prognostic equations are devoted to the microphysics (Lopez 2002). However, the question regarding the level of complexity required to accurately represent cloud and precipitation (and their subsequent effect on the environment) is still open. For instance, Ferrier (1994) or Walko *et al.* (1995) advocate considering four or even five ice categories.

This question motivated our next two experiments. In experiment E2, all the clouds and precipitation are assumed to be liquid, and only the warm microphysical processes were considered. Due to the position of the freezing level (around 3 km), and the cloud-top heights (reaching 12 km), this certainly is a very crude assumption (although it drastically simplifies the computations). Moving in the other direction, it is questionable whether the standard Meso-NH microphysical scheme is sufficiently sophisticated to represent the evolution of the IOP 2a squall line. Tabary (2002) used the particle-type identification algorithm of Vivekanandan *et al.* (1999) to retrieve the microphysical structure of the IOP 2a convective system. His study clearly shows that the main reflectivity cores were associated with a mixture of hail particles and graupel between 18 UTC and 20 UTC and dominantly hail after 20 UTC. The Meso-NH microphysical scheme is not yet fully suited to handling the simultaneous presence of hail and graupel. But to get a rough estimate of the potential impact of hail an additional experiment (E3) was performed in which the graupel characteristics were replaced by those of denser hail particles (see Table 1).

An example of the results obtained with experiments E2 and E3 is presented in Fig. 8. Results are shown only at 20 and 22 UTC. In the case of E2, major differences are the narrowing of the precipitating area, a slower eastward displacement, and a more rapid decay of the system. Such an impact of the ice phase on convective squall lines has

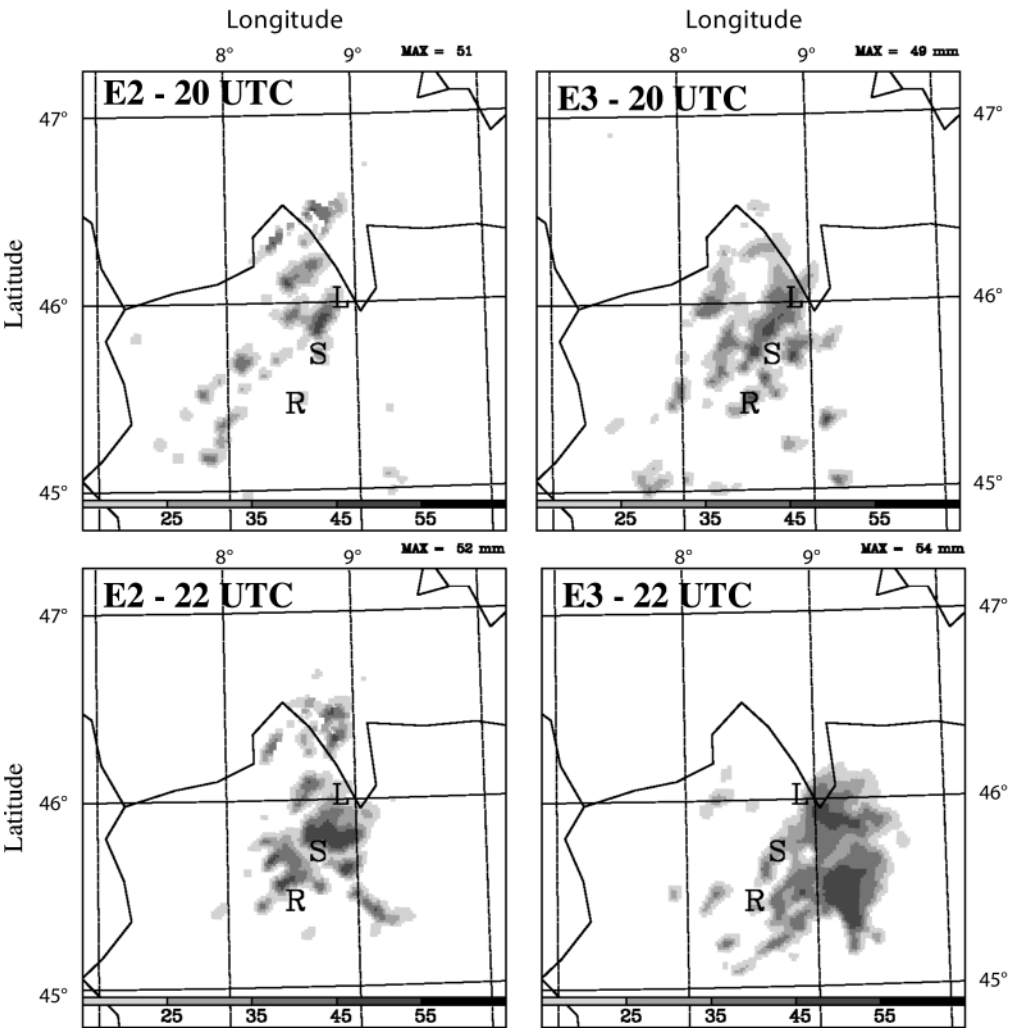


Figure 8. Computed reflectivity fields (dBZ) for 17 September 1999 (20 and 22 UTC) at 2000 m in the Lago Maggiore area: results of experiments E2 (left) and E3 (right). R, S and L as in Fig. 4.

been reported previously (e.g. in Caniaux *et al.* (1994), for a tropical squall line, or in Stein *et al.* (2000), for the Vaison la Romaine 1992 flash-flood episode). It is a classical consequence of the different aerodynamical properties of raindrops and ice particles. Partially glaciated clouds experience a longer life cycle due to the larger residence time of solid hydrometeors and to a different distribution of liquid precipitation (and associated evaporative cooling).

The results obtained with experiment E3 do not depart much from the control experiment but it should be noted that convection is slightly intensified as well as the propagation speed of the system. Compared with raindrops, hail particles are light enough to be advected at the rear of the system where they fall into unsaturated regions and partially evaporate, but they fall faster than graupel leading to a faster depletion of ice inside the precipitating system.

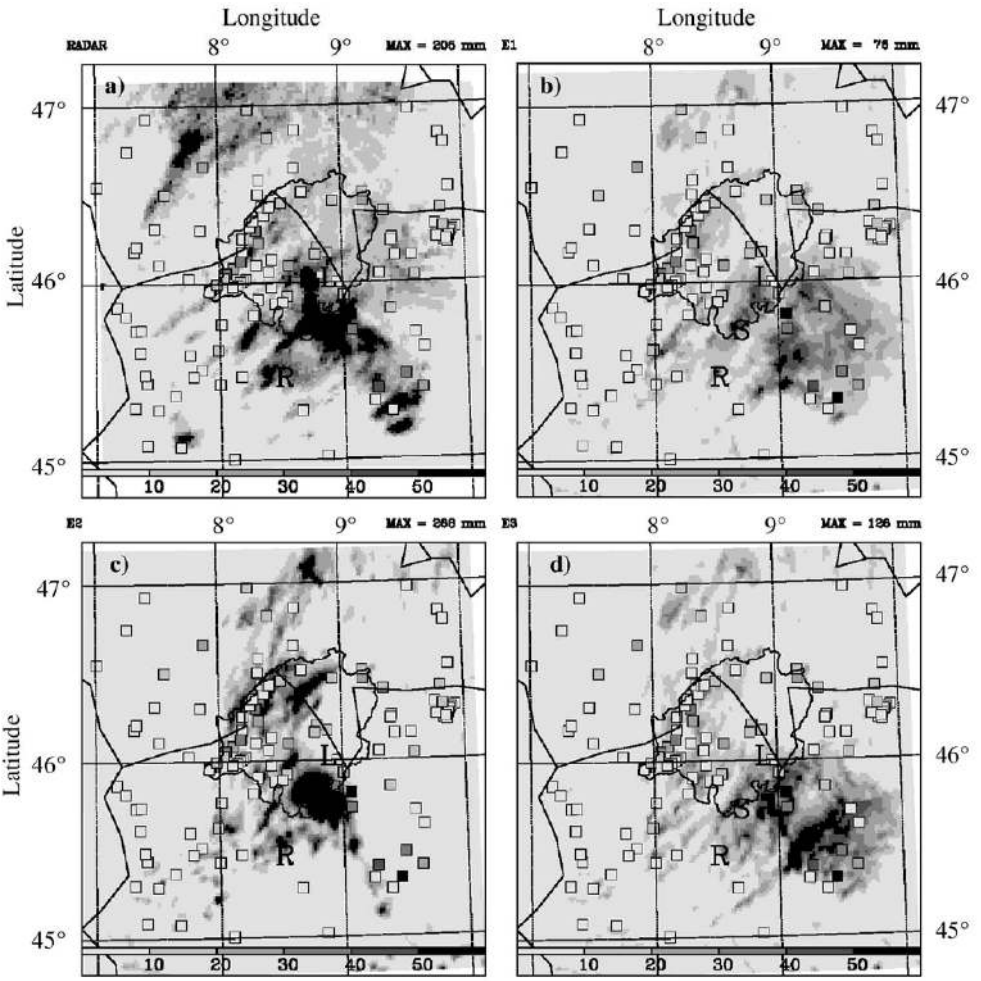


Figure 9. Radar-derived precipitation (mm) accumulated over 12 h (from 17 September 1999, 12 UTC to 18 September 1999, 00 UTC) superimposed on the rain-gauge measurements (indicated by the squares) for the same time period (a). Computed accumulated precipitation over the same 12 h period obtained with the three numerical experiments E1 (b), E2 (c) and E3 (d).

### (*c*) *Precipitation fields*

One major challenge for numerical mesoscale models is of course to achieve the best possible forecast/hindcast of the space and time precipitation distribution. Surprisingly, this quantity, although being a surface meteorological parameter, is still difficult to measure. High-resolution measurements provided by surface rain-gauges are mostly available as daily precipitation sums only, which do not give enough information on the time evolution. Furthermore, the density of the rain-gauge network is highly variable in space and becomes coarser in mountainous areas. Therefore, radar products offer an attractive and complementary alternative for model validation. Both time and space resolutions of radar data are consistent with the ones of high-resolution models.

To assess the quality of our different precipitation simulations, both radar and rain-gauge data were used. About 300 point measurements from the rain-gauge network

are included in the model domain but only one third provide hourly precipitation data. The radar-derived accumulated precipitation was obtained by summing up the precipitation rates of the Swiss radar composite (subset of the Alpine composite but available every 5 min). The computation was made for the 12 h period corresponding to the simulation integration for comparison with model results.

Figure 9(a) shows station measurements superimposed on the radar-derived field. As expected, the maximum precipitation is found in the south-east quarter of the domain. The rain-gauge density is comparatively weak in this area, but there are still a few measurement points giving values between 50 and 60 mm, that are quite consistent with the radar estimates. There is no major discrepancy between station measurements and radar-derived values. We can, therefore, consider that the radar-derived field plotted in Fig. 9(a) gives a reasonably reliable picture of the observed precipitation. It can be compared with the precipitation obtained from our three numerical experiments, plotted on the same figure. Experiment E2 gives the most intense rainfall, but does not catch the south-east spreading of the precipitating area. This feature is better captured in experiments E1 and E3 which account for the ice phase. As already inferred from Figs. 6 and 8, ice particles contribute to sustain the convective system which has a longer life cycle in E1 and E3 than in E2. The two experiments with the ice phase (E1 and E3) produce fairly similar precipitation patterns but the precipitation intensity is significantly increased when graupel is replaced by hail particles.

## 5. Quantitative evaluation

The comparisons with the observations presented so far are still subjective. In order to get a more quantitative and objective assessment of the model results, statistical parameters were systematically computed between the available observations and the different numerical datasets. On one hand, the evaluation is based on the accumulated precipitation at the surface and, on the other hand, on the radar reflectivities in the four-dimensional space. For both, various statistical parameters were computed, such as bias, standard deviation, correlation coefficient, and also various skill scores based upon contingency tables. These latter are supposed to be more informative in the case of semi-bounded variables (like precipitation) for which correlation is not fully meaningful. However, on the limited dataset we are working with, they appeared quite sensitive to the number of points, and to the definition of the class limits. In the following, only the correlation will be discussed, since no additional information was really derived from the skill scores.

### (*a*) *Accumulated precipitation*

For the precipitation evaluation, we used: (i) the rain-gauge measurements from 120 stations providing hourly rainfall, and (ii) the precipitation derived from the Swiss radar composite (61 828 points in the domain, available every 5 min). An alternative would be to use the precipitation derived from the research radar network (RONSARD, S-Pol and Monte Lema) but these data are available only every 15 min. Some tests made with the Swiss radar composite showed that the reliability of the accumulated precipitation is really decreased when the computation is done by integrating the instantaneous precipitation rates with a 15 min time interval instead of a 5 min one. Furthermore, each radar of the operational network benefits from a long time history on which the

TABLE 2. CORRELATION COEFFICIENTS OF THE PRECIPITATION DERIVED FROM THE ALPINE RADAR COMPOSITE AND THE PRECIPITATION COMPUTED IN EXPERIMENTS E1 TO E3 WITH THE PRECIPITATION MEASURED WITH THE SURFACE RAIN-GAUGES (120 POINTS IN THE DOMAIN)

| | Radar | E1 | E2 | E3 |
|---|---|---|---|---|
| Correlation coefficient | 0.69 | 0.32 | 0.07 | 0.34 |
| Mean value over 12 h (mm) | 11.3 | 9.1 | 8.1 | 9.9 |

The last line gives the mean value of each field and can be compared with the mean value of the rain-gauge measurements (10.3 mm).

TABLE 3. CORRELATION COEFFICIENTS BETWEEN THE PRECIPITATION COMPUTED IN EXPERIMENTS E1 TO E3 AND THE PRECIPITATION DERIVED FROM THE ALPINE RADAR COMPOSITE (61 828 POINTS IN THE DOMAIN)

| | E1 | E2 | E3 |
|---|---|---|---|
| Correlation coefficient | 0.46 | 0.43 | 0.47 |
| Mean value over 12 h (mm) | 6.6 | 6.7 | 7.2 |

The last line gives the mean value of each field and can be compared with the mean value of the radar-derived field (11.6 mm).

calibration of the radar-derived precipitation rates* is based. For these different reasons, it was considered that for surface rainfall the Swiss radar composite was more reliable than the Lago Maggiore radar network.

Tables 2 and 3 summarize the statistical analysis. Table 2 compares both the radar and model fields with the rain-gauge measurements. Both fields were interpolated at the surface observation points.

On average, the radar-derived precipitation is higher (11.3 mm for the mean value over the 120 points corresponding to the surface observations points, versus 10.3 mm for the surface observations). The correlation with surface observations is not very strong with a coefficient of only 0.69, confirming thereby the difficulty of getting a true estimate of the surface rainfall in mountainous areas. For the model fields, the mean values (ranging from 8.1 to 9.9 mm) are systematically below the mean rain-gauge value and the correlation coefficients (ranging from 0.07 to 0.34) are also significantly weaker compared with the radar one. If we assume that the rain-gauges give a representative measurement of the surface rainfall, it should be concluded that the radar (model) overestimates (underestimates) the precipitation and that the model fields are not yet as accurate as the radar fields. But probably the most interesting point in Table 2, is the variation between the three numerical experiments. As suggested by Fig. 9, experiment E2 (warm microphysics) provides the worst results (with a correlation coefficient of 0.07), whereas, experiment E3 (with pseudo-hail) tends to be better than the control experiment. The correlation is slightly better and the negative bias is significantly reduced.

* In the Swiss composite, the precipitation rate $R$ is related to the reflectivity $Z$ via the relationship $Z = 316R^{1.5}$ routinely used by MeteoSwiss. For the MAP Special Observing Period, a slightly different relation was found by Hagen and Yuter (2003) but appeared to be quite variable from one event to the other.

Table 3 provides similar information except that the reference is now the radar-derived precipitation. Model fields were interpolated at the 61 828 radar measurement points. The model underestimation is more pronounced and disparities between the numerical simulations are not as clear as in Table 2. Experiment E2 is worse than the other two. The improvement obtained with experiment E3 still exists, but is now rather weak.

### (*b*) *Precipitation time series*

Figure 10 presents the time evolution of the hourly precipitation rates measured by the rain-gauges, derived from the radar observations, and computed with experiments E1, E2 and E3, for six surface stations located within or close to the maximum precipitation core. Even for this subset of stations, located in the plain and not too far from Monte Lema, radar-derived precipitation and gauge measurements do not match perfectly well and may diverge substantially (e.g. in Stabio). Also, some measurements may not be totally correct. For instance, in Como, the time shift between radar and surface observations is suspicious. Concerning computed precipitation, results of experiment E2 are not satisfactory. Precipitation does not occur or occurs too late. Better agreement is obtained for experiments E1 and E3 which capture fairly well the correct intensity and timing of the precipitation peak. In most places, experiment E3 gives significantly better results than E1.

### (*c*) *Reflectivities*

Radar-derived precipitation measurements are very valuable because of their space and time resolution but of course they also have their own limitations (Joss and Lee 1995). First, they suffer from the well known technical difficulties of radar measurements (attenuation, ground masks, ground clutter, . . . ). Second, additional errors arise because reflectivity is not a direct measure of rainfall rate. Therefore, an evaluation directly based upon reflectivity may bypass some sources of uncertainties and moreover allows not only the surface precipitation but also the vertical structure of the precipitating system to be checked.

A similar statistical analysis was conducted to compare the model reflectivity fields with the reflectivity fields measured by the three Doppler radars of the Lago Maggiore area. A composite radar reflectivity was constructed by interpolating on a regular grid (with a 2 km mesh in the horizontal and 500 m in the vertical) the reflectivities of the Monte Lema, S-Pol and RONSARD radars and taking at each grid point the maximum value of the three measurements. The computations were carried out every hour (from 19 UTC to 23 UTC, i.e. for the time period when the convective system was well located above the radar network). Depending upon the selected time and vertical level, the analysis included between 2000 and 7000 grid points per vertical level.

Results are illustrated in Fig. 11 which shows the time evolution of the correlation coefficient between the composite reflectivity and the model reflectivity for the three experiments and for different altitudes. The correlation coefficients are still weak (0.6 at best) but the differences between the various experiments are amplified. Experiment E2 (warm microphysics) is not as good as the control experiment, especially for the levels above the freezing level. Experiment 3 is significantly better than the control experiment. This is particularly clear for the highest level.

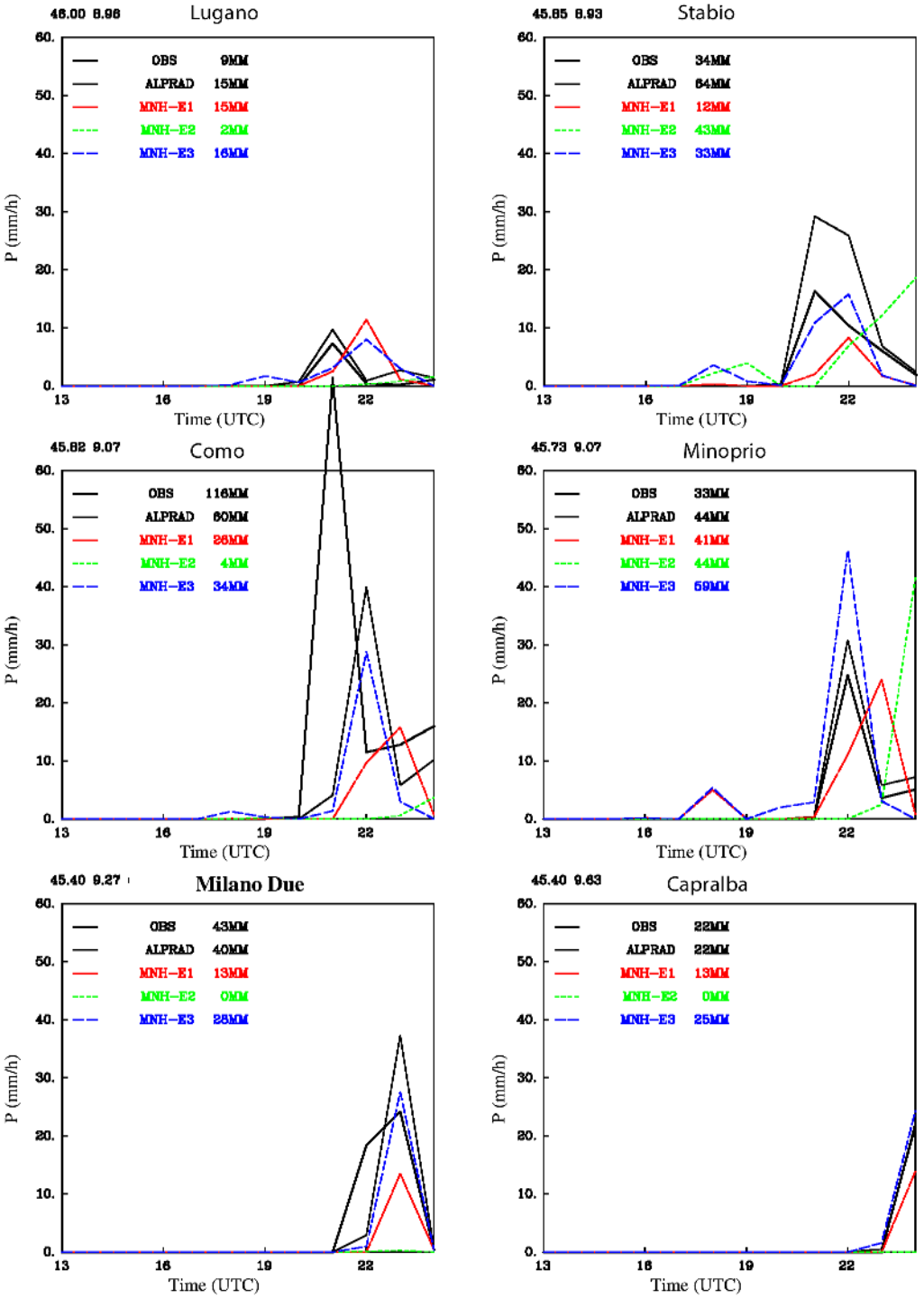


Figure 10. Time evolution of the hourly precipitation rates (P) measured by the rain-gauges (OBS), deduced from the radar measurements (ALPRAD) and computed in experiments E1, E2 and E3 (MNH-E1, MNH-E2, MNH-E3) for six surface stations located in the vicinity of the maximum precipitation core. The latitude, longitude, and name of each surface station is indicated at the top of each frame. (This figure can be seen in colour in the online version.)

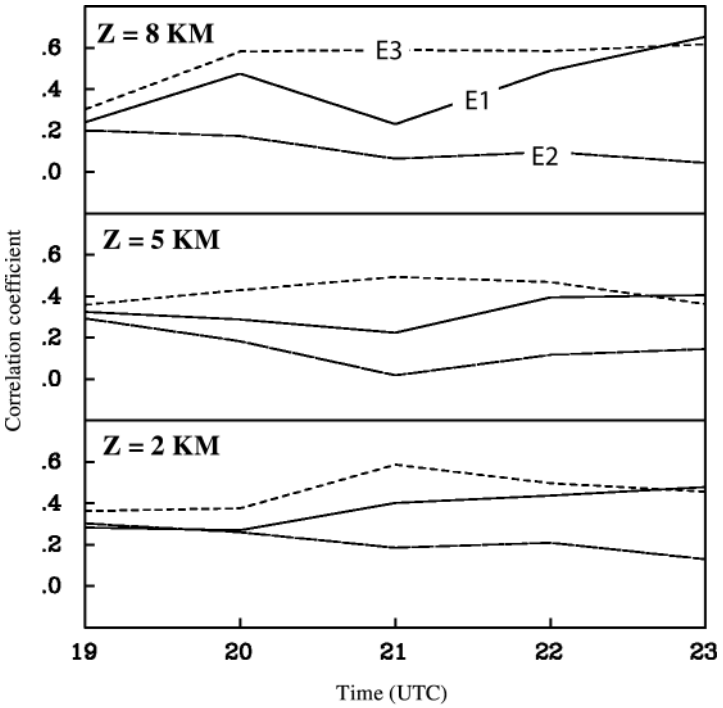


Figure 11. Time evolution of the correlation coefficients between measured and computed reflectivities for the three numerical experiments E1, E2 and E3, and for different heights above sea level.

## 6. Conclusion

Numerical simulations of the MAP IOP 2a convective system were carried out with the Meso-NH model run over three nested domains and with a 2 km horizontal resolution for the finest grid. Several experiments were performed to evaluate the model skill and to explore the sensitivity of the results to the explicit microphysical scheme.

It was found that the ice phase contributes to sustain the convective activity, to increase its lifetime and to accelerate its propagation speed, and yields a better agreement between simulation results and observations. A more minor change in the microphysical scheme, such as replacing the graupel characteristics by those of denser hail particles (more in agreement with the observed hydrometeor types), leads to further improvement of the simulation results.

Radar data were used extensively to provide a qualitative assessment of the computated precipitation. Contrary to rain-gauge measurements they provide not only surface accumulated precipitation but also four-dimensional information on the precipitating system, particularly valuable for model validation. Two radar datasets were employed, one provided by the operational Swiss network, the other by the research radar network of the Lago Maggiore area. The first was used to evaluate the accumulated surface precipitation. On average, the model underestimates the precipitation by 10% whereas the radar overestimates it by 10%. Correlation coefficients between computed precipitation and rain-gauge measurements hardly exceed 0.4 and have to be compared with the 0.7 value obtained with the radar estimates. Despite the apparent realism of the simulations (at least the ones which consider mixed-phase clouds), the numerical results are not yet as accurate as radar-derived estimates.

The second radar dataset was used in a more exploratory way. To by-pass some uncertainties linked to the conversion from reflectivity to precipitation, pseudo radar reflectivities were computed from the model microphysical fields. The quantitative evaluation based upon the reflectivity is consistent with the one obtained for surface precipitation but more informative. It emphasizes the sensitivity of the results to the details of the microphysical scheme. On average, the correlation coefficient is decreased by 0.1 when ice microphysical processes are neglected, and increased by 0.1 when the most heavily rimed particles are considered to be hail particles instead of graupel.

These results will guide our future work. The improvement obtained with the particle-type modification certainly speaks for the inclusion of a specific hail category in the microphysical scheme. But several other lines will be explored to improve the results. Is a 2 km horizontal resolution really sufficient to explicitly resolve the system and/or the topographical forcing? What is the role of the surface processes, especially in the triggering phase? Can we improve the initial analysis by taking advantage of the radar measurements? What will be the impact of the MAP re-analyses (currently underway at ECMWF)?

## Acknowledgements

We gratefully acknowledge all the students and technical staff who contributed to the operation (sometimes in quite difficult conditions) of the radar network of the Lago Maggiore area and especially Serge Prieur who managed to solve many network problems. We thank Jean-François Mahfouf (ECMWF) and Jean Pailleux (Météo-France) for many discussions related to the analysis products, Jacqueline Duron (Laboratoire d'Aérologie) for graphics assistance, and Rosalie Redmond for editorial help.

This study was supported by the Institut National des Sciences de l'Univers (Programme Atmosphère et Océan à Multi-échelles). Computational resources were provided by the Institut du Développement et des Ressources en Informatique Scientifique (under project 950569-CP1). The Deutsche Zentrum für Luft- und Raumfart is gratefully acknowledged for its support to the lead author during an extended stay in Oberpfaffenhofen.

## Appendix

This section describes the computation of the radar reflectivity in the Meso-NH code using a generic representation of the hydrometeor size distributions. It is implicitly assumed that the radar wavelength is large enough that radar waves propagate without attenuation and that the Rayleigh scattering approximation ($\propto D^6$ cross-section efficiency) is valid.

The microphysical scheme assumes that each type of hydrometeor (rain, snow/aggregate, graupel and hail) with an assigned index $i \in$ [r, s, g, h], follows a generalized gamma distribution, given below in the normalized form:

$$n_i(D)\,\mathrm{d}D = N_i\, g_i(D)\,\mathrm{d}D = N_i \frac{\alpha_i}{\Gamma(\nu_i)} \lambda_i^{\alpha_i \nu_i} D^{\alpha_i \nu_i - 1} \exp\{-(\lambda_i D)^{\alpha_i}\}\,\mathrm{d}D \qquad \text{(A.1)}$$

where $D$ is the maximum dimension of the particles, $N_i$ the concentration, $\nu_i$ and $\alpha_i$ are dispersion parameters and $\lambda_i$ the slope parameter. $\Gamma$ is the gamma function (see Press *et al.* (1992) for the coding). The use of the generalized gamma law allows a greater flexibility in representing the particle size distribution while $M(p)$, the $p$th moment of

the law is easily computed as:

$$M_i(p) = \int_0^\infty D^p g_i(D)\,\mathrm{d}D = \frac{G_i(p)}{\lambda_i^p}, \tag{A.2}$$

where

$$G_i(p) = \frac{\Gamma(\nu_i + p/\alpha_i)}{\Gamma(\nu_i)}. \tag{A.3}$$

The one-moment microphysical scheme of Meso-NH assumes that $N_i$ is a power function of $\lambda_i$ (Caniaux *et al.* 1994):

$$N_i = C_i \lambda_i^{X_i}. \tag{A.4}$$

For example, taking $X_i = 0$ means that the total number concentration is held fixed while for $X_i = -1$, it is the intercept parameter ($N_0 \equiv C_i$) of a Marshall–Palmer distribution law (with $\nu_i = \alpha_i = 1$ in Eq. (A.1) to provide the classical form $n(D)\,\mathrm{d}D = N_0\,\mathrm{e}^{-\lambda D}\,\mathrm{d}D$) which is kept constant. The model predicts mixing ratios, $r_i$ which are expressed from Eq. (A.1) and the mass–diameter relationship ($m(D) = a_i D^{b_i}$):

$$\rho_{\mathrm{dref}} r_i = \int_0^\infty m(D) n_i(D)\,\mathrm{d}D = a_i N_i M_i(b_i) \tag{A.5}$$

where $\rho_{\mathrm{dref}}$ is the dry-air reference density of the anelastic system of equations. Using Eqs. (A.4), (A.2) and (A.5), it is possible to compute the slope parameter $\lambda_i$ as:

$$\lambda_i = \left(\frac{\rho_{\mathrm{dref}} r_i}{a_i C_i G_i(b_i)}\right)^{\frac{1}{X_i - b_i}}. \tag{A.6}$$

The total equivalent radar reflectivity factor $Z_{\mathrm{e}}$ (dBZ), is calculated as a sum of radar reflectivities produced by each hydrometeor type which is illuminated by the radar wave (Ferrier 1994):

$$Z_{\mathrm{e}} = \log_{10}(Z_{\mathrm{er}} + Z_{\mathrm{es}} + Z_{\mathrm{eg}} + Z_{\mathrm{eh}}). \tag{A.7}$$

The rain contribution, $Z_{\mathrm{er}}$ has the simplest form

$$Z_{\mathrm{er}} = 10^{18} \int_0^\infty n_{\mathrm{r}}(D) D^6\,\mathrm{d}D \tag{A.8}$$

which is integrated using Eqs. (A.2) and (A.3), to give:

$$Z_{\mathrm{er}} = 10^{18} C_{\mathrm{r}} G_{\mathrm{r}}(6) \lambda_{\mathrm{r}}^{x_{\mathrm{r}}-6}. \tag{A.9}$$

The case of ice particles is a little bit more difficult to treat because one must consider the melted diameter of the particles ($D_{\mathrm{e}}$) and also the possible partial coating of these particles by a liquid film. The last effect is important because solid ice has a reduced specific dielectric factor of 0.224 which explains, for instance, the formation of a bright band when the snowflakes are falling across the melting level.

For the snow/aggregate category, $Z_{\mathrm{es}}$ is thus given by

$$Z_{\mathrm{es}} = 10^{18} \int_0^\infty 0.224 n_{\mathrm{s}}(D_{\mathrm{e}}) D_{\mathrm{e}}^6\,\mathrm{d}D_{\mathrm{e}} \tag{A.10}$$

with $D_{\mathrm{e}}$ deduced from

$$m_i(D) = a_i D^{b_i} = \frac{\pi}{6} \rho_{\mathrm{w}} D_{\mathrm{e}}^3 = m_{\mathrm{r}}(D_{\mathrm{e}}) \tag{A.11}$$

where $\rho_w$ stands for liquid-water density, so inserting Eq. (A.11) into Eq. (A.10) with $n_s(D)\,\mathrm{d}D = n_s(D_e)\,\mathrm{d}D_e = n_s\{D_e(D)\}\,|\partial D_e/\partial D|\,\mathrm{d}D$ and performing the integration of Eq. (A.10) yields

$$Z_{es} = 0.224 \times 10^{18} \left(\frac{b_s}{3}\right) \left(\frac{6}{\pi}\frac{a_s}{\rho_w}\right)^{\frac{7}{3}} C_s G_s \left(\frac{7b_s}{3} - 1\right) \lambda_s^{X_s - \frac{7b_s}{3}+1}. \tag{A.12}$$

The snow category is composed of large ice crystals and of dry assemblages of smaller ice crystals. Only a small amount of light rime is allowed for these particles because they are converted into densely rimed graupel when much supercooled water is collected. Furthermore, the snowflakes are progressively converted into graupel-like hydrometeors when they go through the melting level. So it is assumed that the snow/aggregate category is exclusively composed of dry ice without unfrozen liquid water.

The equivalent radar reflectivity factor of the graupel, $Z_{eg}$ is given by

$$Z_{eg} = \begin{cases} 10^{18} \displaystyle\int_0^\infty \{0.224(1 - f_c) + f_c\}\, n_g(D_e) D_e^6\, \mathrm{d}D_e & \text{for } T < 273.16\ \mathrm{K}, \\ 10^{18} \displaystyle\int_0^\infty n_g(D_e) D_e^6\, \mathrm{d}D_e & \text{for } T > 273.16\ \mathrm{K}, \end{cases} \tag{A.13}$$

with again $D_e$ defined by Eq. (A.11). The water coating factor $f_c$ was set to an empirical constant value of 0.14 as suggested by Rasmussen *et al.* (1984). The same was done by Walko *et al.* (1995) to compute the shedding rate of the hailstones. It is assumed also that the graupel are fully wetted hydrometeors below the melting level ($T > 273.16$ K). Integration of Eq. (A.13) leads to

$$Z_{eg} = \begin{cases} \{0.224(1 - 0.14) + 0.14)\}\times \\ 10^{18} \left(\frac{b_g}{3}\right) \left(\frac{6}{\pi}\frac{a_g}{\rho_w}\right)^{\frac{7}{3}} C_g G_g \left(\frac{7b_g}{3} - 1\right) \lambda_g^{X_g - \frac{7b_g}{3}+1} & \text{for } T < 273.16\ \mathrm{K}, \\ 10^{18} \left(\frac{b_g}{3}\right) \left(\frac{6}{\pi}\frac{a_g}{\rho_w}\right)^{\frac{7}{3}} C_g G_g \left(\frac{7b_g}{3} - 1\right) \lambda_g^{X_g - \frac{7b_g}{3}+1} & \text{for } T > 273.16\ \mathrm{K}. \end{cases} \tag{A.14}$$

The equivalent reflectivity of hail $Z_{eh}$ is simply given by:

$$Z_{eh} = 10^{18} \left(\frac{b_h}{3}\right) \left(\frac{6}{\pi}\frac{a_h}{\rho_w}\right)^{\frac{7}{3}} C_h G_h \left(\frac{7b_h}{3} - 1\right) \lambda_h^{X_h - \frac{7b_h}{3}+1} \tag{A.15}$$

because it is assumed that the hailstones are fully coated by a liquid film as a result of the 'wet mode' growth of these particles with a continuous water shedding.

## References


Arakawa, A. and Mesinger, F. 1976 'Numerical methods used in atmospheric models'. GARP Tech. Rep., **17**

Asselin, R. 1972 Frequency filter for time integrations. *Mon. Weather Rev.*, **100,** 487–490

Bechtold, P., Bazile, E., Guichard, F., Mascart, P. and Richard, E. 2001 A mass flux convection scheme for mesoscale and global models. *Q. J. R. Meteorol. Soc.*, **126,** 865–889

Benoit, R., Desgagné, M., Pellerin, P., Desjardins, S. and Chartier, Y. 1997 The Canadian MC2: A semi-Lagrangian, semi-implicit wideband atmospheric model suited for fine-scale process studies and simulations. *Mon. Weather Rev.*, **125,** 2382–2415

Benoit, R., Schär, C., Binder, P., Chamberland, S., Davies, H. C., Desgagné, M., Girard, C., Keil, C., Kouwen, N., Luthi, D., Maric, D., Muller, E., Pellerin, P., Schmidli, J., Schubiger, F., Schwierz, C., Spenger, M., Walser, A., Willemse, S., Yu, W. and Zala, E. 2002 The realtime ultrafinescale forecast support during the special observing period of the MAP. *Bull. Am. Meteorol. Soc.*, **83,** 85–109

Bielli, S. and Roux, F. 1999 Initialization of a non-hydrostatic cloud model with wind and reflectivity fields derived from airborne Doppler radar data. *Mon. Weather Rev.*, **127,** 1038–1055

Bougeault, P. and Lacarrère, P. 1989 Parameterization of orographic induced turbulence in a mesobeta scale model. *Mon. Weather Rev.*, **117,** 1872–1890

Bougeault, P., Binder, P., Buzzi, A., Dirks, R., Houze, R., Kuettner, J., Smith, R. B., Steinacker, R. and Volkert, H. 2001 The MAP Special Observing Period. *Bull. Am. Meteorol. Soc.*, **82,** 433–462

Caniaux, G., Relelsperger, J. L. and Lafore, J. P. 1994 A numerical study on the stratiform region of a fast moving squall line. Part I: General description and water and heat budget. *J. Atmos. Phys.*, **51,** 2046–2073

Chen, S. and Cotton, W. R. 1988 The sensitivity of a simulated extratropical mesoscale convective system to longwave radiation and ice-microphysics. *J. Atmos. Sci.*, **45,** 3897–3910

Chin, H. N. S. 1994 The impact of the ice phase and radiation on a midlatitude squall line system. *J. Atmos. Sci.*, **51,** 3320–3343

Chong, M., Georgis, J. F., Bousquet, O., Brodzik, S. R., Burghart, C., Cosma, S., Germann, U., Gouget, V., Houze, R. A., James, C. N., Prieur, S., Rotunno, R., Roux, F., Vivekanandan, J. and Zheng, Z. X. 2000 Real-time wind synthesis from Doppler radar observations during the Mesoscale Alpine Programme experiment. *Bull. Am. Meteorol. Soc.*, **81,** 2953–2962

Ferrier, B. S. 1994 A double-moment multiple phase four-class bulk ice scheme. Part I: Description. *J. Atmos. Sci.*, **51,** 249–280

Gal-Chen, T. and Sommerville, R. C. J. 1975 On the use of a coordinate transformation for the solution of the Navier-Stokes equations. *J. Comput. Phys.*, **17,** 209–228

Hagen, M. 1999 'The Alpine radar composite'. Pp. 20–21 in MAP Newsletter No. 11. Meteoswiss, CH-8044, Zurich, Switzerland

Hagen, M. and Yuter, S. E. 2003 Relations between radar reflectivity, liquid-water content, and rainfall rate during the MAP SOP. *Q. J. R. Meterolol. Soc.*, **129,** 477–493

Houze, R. A., Curtis, N. J. and Medina, S. 2001 Radar observations of precipitation and airflow on the Mediterranean side of the Alps: Autumn 1998 and 1999. *Q. J. R. Meteorol. Soc.*, **127,** 2537–2558

Joss, J. and Lee, R. 1995 The application of radar-gauge comparisons to operational precipitation profile corrections. *J. Appl. Meteorol.*, **34,** 2612–2630

Kain, J. S. and Fritsch, J. K. 1993 Convective parameterization for mesoscale models: The Kain–Fritsch scheme. *Meteorol. Monogr.*, **46,** 165–170

Krueger, S. K., Fu, Q., Liou, K. N. and Chin, H. N. S. 1995 Improvements of an ice-phase microphysics parameterization for use in numerical simulations of tropical convection. *J. Appl. Meteorol.*, **34,** 281–287

Lafore, J. P., Stein, J., Bougeault, P., Ducrocq, V., Duron, J., Fischer, C., Héreil, P., Mascart, P., Masson, V., Pinty, J. P., Redelsperger, J. L., Richard, E. and Vilà-guerau de Arellano, J. 1998 The Meso-NH atmospheric simulation system. Part I: Adiabatic formulation and control simulations. *Annales Geophysica*, **16,** 90–109

Leise, J. A. 1981 'A multidimensional scale-telescoped filter and data extension package'. NOAA Tech. Memo., **ERL/WPL-82**

Lilly, D. K. 1990 Numerical prediction of thunderstorms—has its time come? *Q. J. R. Meteorol. Soc.*, **116,** 779–798

Lipps, F. B. and Hemler, R. S. 1982 A scale analysis of deep moist convection and some related numerical calculations. *J. Atmos. Sci.*, **39,** 2192–2210

Lopez, P. 2002 Implementation and validation of a new prognostic large-scale cloud and precipitation scheme for climate and data assimilation purposes. *Q. J. R. Meteorol. Soc.*, **128,** 229–258

McCumber, M., Tao, W. K., Simpson, J., Penc, J. and Soong, S. T. 1991 Comparison of ice-phase microphysical parameterization schemes using numerical simulations of tropical convection. *J. Appl. Meteorol.*, **30,** 985–1004

Morcrette, J. 1989 'Description of the radiation scheme in the ECMWF model'. ECMWF Tech. Memo., **165**

Noilhan, J. and Planton, S. 1989 A simple parameterization of land surface processes for meteorological models. *Mon. Weather Rev.*, **117,** 536–549

Pinty, J. P. and Jabouille, P. 1998 'A mixed-phase cloud parameterization for use in a mesoscale non hydrostatic model: Simulations of a squall line and of orographic precipitation'. Pp. 217–220 in Proceedings of the conference on cloud physics, 17–21 August 1998, Everett, Wa, USA

Press, W. H., Teukolsky, S. A., Vetterling, W. T. and Flannery, B. P. 1992 *Numerical recipes in FORTRAN: The art of scientific computing. 2nd Ed.* Cambridge University Press

Rasmussen, R. M., Levizzani, V. and Pruppacher, H. R. 1984 A wind tunnel and theoretical study on the melting behavior of atmospheric ice particles. III: Experiment and theory for spherical ice particles of radius $> 500$ $\mu$m. *J. Atmos. Sci.*, **41,** 381–388

Stein, J., Richard, E., Lafore, J. P., Pinty, J. P., Asencio, N. and Cosma, S. 2000 Meso-NH simulations with grid-nesting and ice phase parameterization. *Meteorol. Atmos. Phys.*, **72,** 203–221

Tabary, P. 2002 'Observations radar de systèmes précipitants orographiques pendant l'expérience MAP'. Thèse de l'Université Paul Sabatier

Vivekanandan, J., Zrnic, D. S., Ellis, S. M., Oye, R., Ryzhkov, A. V. and Straka, J. 1999 Cloud microphysics retrieval using S-Band dual-polarization radar measurements. *Bull. Am. Meteorol. Soc.*, **80,** 381–388

Walko, R. L., Cotton, W. R., Meyers, M. P. and Harrington, J. Y. 1995 New RAMS cloud microphysics parameterization. Part I: The single-moment scheme. *Atmos. Res.*, **38,** 29–62

Yang, M. J. and Houze, R. A. 1995 Sensitivity of squall-line rear inflow to ice microphysics and environmental humidity. *Mon. Weather Rev.*, **123,** 3175–3193